

Banner appropriate to article type will appear here in typeset article

# Wavy-wall-based flow control for the suction side geometry of NACA4412 at $Re_\tau \approx 3000$

Artur Drózd<sup>1</sup>†, Mathias Romańczyk<sup>1</sup> and Witold Elsner<sup>1</sup>

<sup>1</sup>Czestochowa University of Technology, Department of Thermal Machinery, Armii Krajowej 21, 42-200, Czestochowa, PL

(Received xx; revised xx; accepted xx)

The paper presents a high Reynolds number experimental study of turbulent boundary layer separation control on a convex plate using the wavy-wall method, which was initially proposed for a flat plate by Drózd *et al.* 2021 (Exp Therm Fluid Sci 2021;121:110291). The application of this method increases the friction coefficient by up to 42.3%, resulting in a substantial delay in turbulent separation from the convex wall, while maintaining total momentum, quantified by changes in momentum-loss thickness. Other parameters indicating the high efficiency of the method are the invariant value of the friction Reynolds number along the flow and the thinner boundary layer. The above indicators demonstrate promising aerodynamic improvements in airfoils, similar to those achieved when active suction is applied to the suction side. The new insight into the physical mechanism of the wavy wall suggests that small-scale turbulent activity is the primary determinant of the effectiveness of the wavy wall in enhancing small-scale streamwise convection and the sweeping motion, resulting in superior momentum transport. However, when the wavy wall, due to poorly selected geometry, induces large-scale motions, such as separation in the trough, it counteracts the mechanism. Then this geometry has a detrimental effect on the efficiency of the method.

**Key words:** turbulent boundary layers, drag reduction, boundary layer separation

## 1. Introduction

Most passive flow control strategies for aerofoils are based on reducing skin friction by attenuating large-scale streaks (Ricco *et al.* 2021). To mitigate skin friction reduction, which acts as a laminar-turbulent transition postponer, active methods are employed to counteract its detrimental effect on lift due to earlier separation. However, the use of active methods is limited in wind turbine blades due to a combination of practical, aerodynamic, and economic constraints. A commonly applied passive method in wind energy is the use of vortex generators. However, in large-scale wind turbine blades, vortex generators provide only minimal benefits (only about a 1% power increase on 5MW wind turbine blades). They may even lower efficiency at higher power levels (Bravo-Mosquera *et al.* 2022). Alternative passive flow control methods such as dimples (Tay *et al.* 2015; Gattere *et al.* 2022; Aoki

† Email address for correspondence: artur.drozd@pcz.pl

*et al.* 2012; Bearman & Harvey 1976; Tay 2011), grooves (S. & H. 2016), slotted airfoils (Belamadi *et al.* 2016; Coder & Somers 2020; Tanürün *et al.* 2026), or microcylinders (Wang *et al.* 2018; Mostafa *et al.* 2022; Wang *et al.* 2023) have been shown to reduce drag by speeding up the transition; however, their effectiveness diminishes in turbulent flows with high Reynolds numbers as shown by McMasters & Henderson (1979).

A promising alternative is the use of a streamwise wavy wall (WW) with appropriately selected geometry that yields an increase in friction coefficient downstream of WW of more than 35% at the friction Reynolds number  $Re_\tau \approx 4000$  (Drózdź *et al.* 2025). This is the highest reported gain for such a configuration to date, which highlights the practical potential of this method to delay separation. To be effective, the WW design must be carefully tailored to local flow conditions. The undulations should be placed where the Rotta-Clauser pressure gradient parameter  $\beta = \delta^* \tau_w^{-1} dP_e$ , where  $\delta^*$  is displacement thickness,  $\tau_w$  is wall shear stress and  $dP_e$  is streamwise pressure gradient, remains below 10, with a maintained viscous scaled amplitude of  $A^+ = 170$ , and a period adjusted so that flow troughs are held on the verge of separation (effective slope around 0.15). The wavy wall increases the momentum transport due to increased small-scale sweeping motions, in a mechanism similar to amplitude modulation in high-Reynolds wall-bounded flows (Mathis *et al.* 2009; Drózdź *et al.* 2023). Simulations at about  $Re_\tau \approx 2500$  by Kamiński *et al.* (2024) confirmed that the technique can enhance the wall-normal velocity gradient and wall shear stress downstream, although to a lesser extent. In turn, combined numerical LES and wind-tunnel studies by Elsner *et al.* (2022) at  $Re_\tau \approx 1400$  did not show any improvements, suggesting the approach loses efficacy below a certain threshold Reynolds number.

The recent work of Drózdź *et al.* (2025) aimed to test the single geometry of the WW selected in Drózdź *et al.* (2021) on a range of Reynolds numbers ( $Re_\tau \approx 2600, 4000, \text{ and } 4500$ ) and under varying pressure gradient conditions corresponding to large-scale pitch-regulated wind turbine blades. For such turbines, the angle of attack varies from  $3^\circ$  to  $8^\circ$  Sayed *et al.* (2012) for different wind speeds, and even more due to the rotational position or torsional deflection of the blade. The results showed that when the Reynolds number varies, as when the wind speeds change from  $5$  to  $40 \text{ m s}^{-1}$  on a pitch-regulated wind turbine, the lowest increase in  $C_f$  was 30% for the lowest Reynolds number. Furthermore, when the pressure gradient was varied at a constant Reynolds number, mimicking unstable flow conditions resulting from changes in the rotational position of the blade or torsional deflection, the efficiency of the wavy wall was maintained, albeit at a lower level of  $C_f$ , about 27% on average. The tested pressure ranges and the Reynolds number variation showed that too low an amplitude limits the benefits. However, too high an amplitude leads to significant separation, which weakens the transport of momentum to the wall. However, as demonstrated, an overall effectiveness of approximately 23% was achieved, which can be considered high.

Recently, large-eddy simulations at  $Re_\tau \approx 2500$  by Kamiński *et al.* (2025) was published as an extended work of Kamiński *et al.* (2024). They showed that the additional benefit can be achieved using the upstream tilted wavy wall (Kamiński *et al.* 2025). They report an increase in wall shear stress with respect to a sinusoidal type of wavy wall. However, the increase is at the level of 40% of that observed in Drózdź *et al.* (2021) due to the lower Reynolds number. On the other hand, Kamiński *et al.* (2025) presented their observations on the physical interpretation of introducing a wavy wall on the curved surface of the NACA4412 wing section. They found that a sinusoidal wavy wall used at  $Re_\tau \approx 2500$  causes increased energy across all scales in the outer region. In contrast, near the wall, only large-scale activity is enhanced, despite the small-scale contribution observed by Drózdź *et al.* (2021).

The experimental results in this paper document for the first time the application of the wavy wall on a convex surface that resembles a wind turbine blade surface at a high Reynolds number  $Re_\tau \approx 3100$  corresponding to the wind speed  $10 \text{ m s}^{-1}$  that occurs on a large-scale

wind turbine blade that spins at a constant speed regulated by the blade pitch. The changes in velocity statistics and boundary-layer parameters produced by the method were compared with those obtained using the active techniques reported in the literature (Atzori *et al.* 2020). New insights into the wavy-wall-induced mechanism are provided based on newly obtained data and already published LES simulations.

## 2. Experimental setup

The experiment was conducted in a modular wind tunnel located at the Czestochowa University of Technology. It was explicitly designed to study the surfaces of the wind turbine blades under real atmospheric conditions, where the canonical turbulent boundary layer can develop without tripping along a 7500mm flat plate (see Figure 1). The Reynolds number based on developing distance is  $Re_x = 10^7$  characteristic for a flow over a 2.0 m chord wind turbine blade under a velocity inlet  $80ms^{-1}$ . Such a condition occurs for an average wind speed of about  $10ms^{-1}$ . The honeycomb-equipped settling chamber, five turbulence grids, and the contraction channel of contraction ratio of 4.5 ensure that the turbulence intensity in the inlet plane was not higher than 0.45%. To mitigate the three-dimensional effects, i.e., secondary flows in the channel, the cross-section of the channel at the inlet was designed with the following  $W \times H$  dimensions: 800 × 416 mm. Downstream of the inlet plane, a curved surface section corresponding to the NACA4412 profile's suction side, positioned at an angle of attack (AoA) of  $5^\circ$ , was installed (see Figure 1). The upper wall of the inlet and airfoil section was inclined at  $0.35^\circ$  to ensure maintaining the ZPG conditions within the inlet section (see Figure 1a). The two-dimensional WW section, where the waviness was extruded along the spanwise direction (800 mm), has a total length of  $L = 540$  mm (4 periods streamwise with  $\lambda = 135$  mm). The wavy wall was manufactured from a high-density polyurethane plate to ensure a smooth hydraulic surface after mechanical processing. After machining, the plate was bent to follow the convex surface curvature.

The amplitude of WW  $A(x)$  increases downstream of the flow according to the relationship:  $A^+ = A(x)u_\tau \nu^{-1} = 170$ , where  $u_\tau$  is the friction velocity and  $\nu$  is the kinematic viscosity. The distributions of the pressure coefficient  $C_P = 1 - U_e^2 U_{e,in}^{-2}$  are shown in Figure 1b. It should be emphasised that the waviness, due to its low amplitude in relation to the height of the channel, does not affect the pressure distribution in the freestream. The experiment was carried out for the value of the inlet velocity  $U_{e,in} \approx 14.5ms^{-1}$ , which corresponds to  $Re_\tau \approx 3100$ .

The StreamlinePro DANTEC hot wire anemometer (HWA) was used at an overheating ratio of 1.8. Two HWA probes were used. The first probe used for measurement on an unmodified surface was the standard gold-plated 55P05 with a wire sensing length of  $l = 1.2mm$  and diameter of  $5 \mu m$ . In that case, not all profiles are free from spatial averaging (see Table 3 and Appendix A). In the case of a wavy wall, an increase in friction velocity occurs; therefore, a modified 55P31 probe was used, with a wire sensing length of  $l = 0.41mm$  and a diameter of  $3 \mu m$ . Such wire dimensions ensured maintaining the nondimensional wire length  $l^+ = lu_\tau \nu^{-1} < 9$ . Data acquisition was performed with sampling frequencies from 25 kHz for profiles taken above  $x = 900mm$  and 50kHz for profiles on the unmodified wing surface up to this location. The temperature variation during the measurement of each velocity profile was not higher than  $\pm 0.2$  K. The flow temperature was used to correct the voltage signal from the hot-wire.

The friction velocity values  $u_\tau = \sqrt{\tau_w / \rho}$ , where  $\tau_w = \mu dU/dy$  and  $\mu$  is the dynamic viscosity and  $dU/dy$  is the wall-normal streamwise velocity gradient at the wall, were estimated using the approach proposed by Niegodajew *et al.* (2019). The uncertainty of the

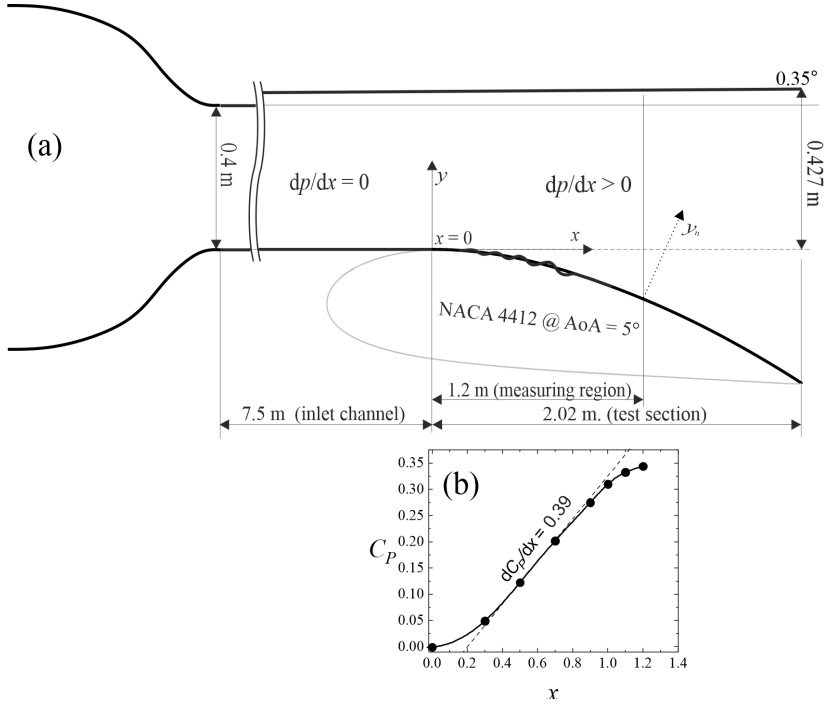


Figure 1: Schematic of the test section (a) and  $C_p$  distributions (b)

Table 1: Inlet TBL parameters

$z$ (m)	$U_{e,in}$ ( $ms^{-1}$ )	$\delta_{in}$ (mm)	$C_{f,in}$ (-)	$\delta_{in}^*$ (mm)	$\theta_{in}$ (mm)	$H_{in}$ (-)	$u_{\tau,in}$ ( $ms^{-1}$ )
○ -0.2	14.58	98.4	0.00255	15.21	11.41	1.333	0.520
○ -0.1	14.32	93.5	0.00259	14.33	10.74	1.334	0.515
○ 0	14.33	90.5	0.00256	14.45	10.74	1.345	0.513
○ 0.1	14.34	93.5	0.00255	14.75	11.00	1.341	0.512
○ 0.2	14.48	91.9	0.00259	14.24	10.67	1.334	0.522

friction velocity, verified against the oil-film interferometry, was up to 2.5% for profiles characterised by shape factor  $H < 2.0$  and up to 5.0% for  $H > 2.0$ .

The uncertainties in the measurement/estimation of  $U$  and  $H$  were below the level of  $0.01U_{e,in}$  and 1.5%, respectively, in the uncertainty of the position of the probe wire in the normal direction of the wall  $\Delta y_m = 0.06$  mm.

### 3. Inlet conditions.

Table 1 contains inlet data for five velocity profiles distributed spanwise. For each case, a ○ symbol colour has been assigned. It is important to note that the flow maintains well-behaved ZPG TBL flow conditions introduced by Sanmiguel Vila *et al.* (2017), as the skin friction coefficient  $C_f$  and the shape factor  $H$  for analysed  $Re_{\theta,in} \approx 9700$  in the inner 50% of channel

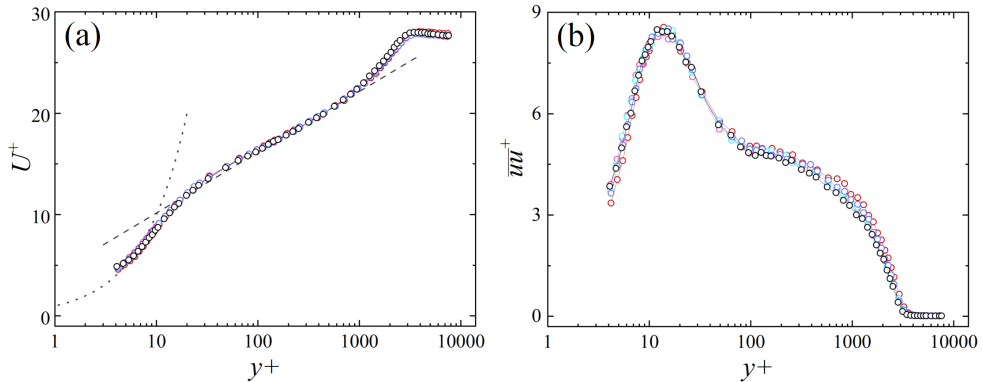


Figure 2: Mean velocity (a) and turbulence intensity (b) profiles presented in viscous scale at  $x = 0$ . The dashed line represents the logarithmic law (with  $\kappa = 0.38$  and  $B = 4.1$ ) while the dotted line represents  $y^+ = U^+$ .

span do not exceed  $\pm 2\%$  and  $\pm 1$  of the Coles–Fernholz formula and the relation proposed by Monkewitz *et al.* (2007), respectively (see Figure (2a)).

Figure 2 shows the inlet profiles ( $x = 0.0$  mm) of the mean velocity  $U^+ = U u_\tau^{-1}$  (2a) and the streamwise Reynolds stresses  $\overline{uu}^+$  in the viscous units (2b), measured for five spanwise locations  $z = -200, 100, 0, 100$  and  $200$  mm. Figure 2a) shows a canonical turbulent boundary layer at the inlet, while Figure 2b) shows that  $\overline{uu}^+$  collapses under uncertainty of 5%. It confirms that the velocity profiles at the inlet were measured using a sufficiently short wire length to avoid small-scale energy attenuation.

## 4. Results

### 4.1. Performance assessment of the method.

In Figure 3, the skin friction coefficient  $C_f = 2u_\tau^2 U_e^{-2}$  for the wavy surface (open symbols) is compared to the unmodified wing surface  $C_f$  (dark symbols), where a second-order polynomial extrapolated the distributions to predict the separation point. The streamwise distance from the inlet  $x$  was reduced by the boundary layer thickness at the inlet  $\delta_{in}$ . The selected purple area indicates the flow region where the waviness is located. Figure 3 illustrates a marked enhancement in the skin-friction coefficient for the wavy wall configuration, as denoted by the open symbols. This increase is accompanied by a pronounced downstream displacement of the turbulent boundary layer separation point, indicating the efficacy of the wavy geometry in delaying flow detachment.

For a more statistically confident estimate of the effect of waviness on the skin friction coefficient, the differences between the  $C_f$  distributions were integrated from the end of the wavy wall to the flow separation location occurring for the flow without surface modification. The integration area does not account for the tangential separation shift  $\Delta x_{t,s}$ . The percentage value of  $\Delta C_f$  was scaled by  $C_{f,in}$  to assess the real effectiveness of the method.

The data in Table 2 show that the selected corrugation geometry produces a 13.4% increase in  $C_f$ , while reducing by value at the inlet  $C_{f,in}$  (quantified in a way presented in Drózdź *et al.* (2021); Drózdź *et al.* (2025)), which translates to an increase of 42.3% in the integration area downstream of the wavy wall (quantified as in Kamiński *et al.* (2025)).

The impact of pressure drag on overall airfoil efficiency remains a pertinent issue. In particular, Kamiński *et al.* (2025) demonstrated that the overall pressure drag induced by the

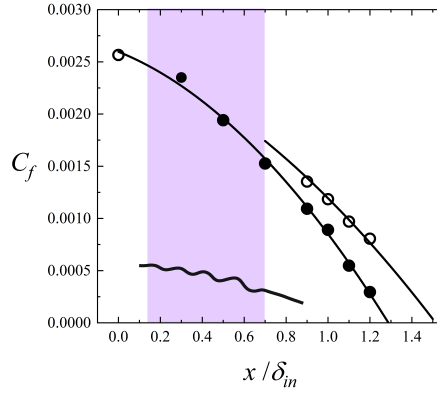


Figure 3: Comparison of skin-friction coefficient distributions. The open symbol corresponds to the wavy wall, while the dark symbol corresponds to the unmodified wing surface.

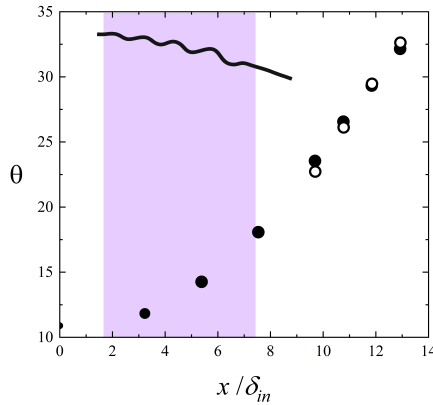


Figure 4: Comparison of momentum loss thickness distributions. The open symbol is marked as a wavy wall case, while dark symbols correspond to the unmodified wing surface.

Table 2: Integrated  $C_f$  difference

Integration area [m]	$\Delta x_{t,s}$ [m]	$\Delta x_{t,s} \delta_{in}^{-1}$ [-]	$\Delta C_f$ [-]	$\Delta C_f$ [%]	$\Delta C_f C_{f,in}^{-1}$ [%]
0.7 - 1.3	0.21	2.32	0.000348	42.3	13.5

wavy wall is 0.00195, which increases the drag coefficient  $C_D$ . However, this is valid only for internal flows. In the case of airfoils, the velocity deficit in the wake determines the drag coefficient.

To assess the reduction in velocity deficit in the wake of the airfoil, it is instructive to examine the evolution of the momentum-loss thickness,  $\theta$ . An effective separation control

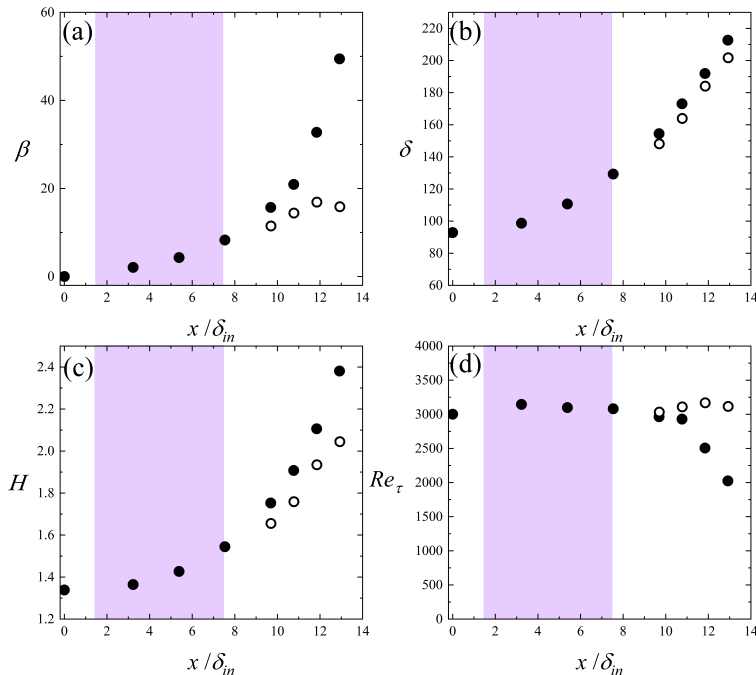


Figure 5: Comparison of  $\beta$  a),  $\delta$  b),  $H$  c) and  $Re_\tau$  d) downstream the flow.

strategy should not merely redistribute momentum toward the wall but rather preserve or enhance the total momentum within the boundary layer. In this context,  $\theta$  serves as a robust integral measure for quantifying the net momentum retention downstream of the control intervention. In Figure 4, the distributions of  $\theta$  for the wavy surface (open symbols) are compared with the distributions of  $\theta$  as a function of  $x\delta_{in}^{-1}$  on the unmodified wing surface (dark symbols). Symbols as in Figure 3.

The results shown in Figure 4 indicate a maintenance of overall momentum by the wavy wall. The wake behind the airfoil defined in the plane perpendicular to the main flow direction, resulting from the boundary layer developing on the suction and pressure sides of the airfoil. Since the thickness of the boundary layer for this location is approximately 5% lower (see Figure 5), the increase in the linear measure of momentum-loss thickness observed in the final profile (at  $x = 1200$  mm) does not directly translate into an increase in the width of the wake. In addition, the wake velocity deficit is influenced by the mixing of boundary layers from the airfoil's upper and lower surfaces. The wavy geometry reduces this mixing by enhancing momentum near the wall on the upper surface, thereby minimising the imbalance between the two boundary layers.

According to Atzori *et al.* (2020), who studied suction and blowing applied on the suction side of the airfoil, an 11% increase in the lift-to-drag ratio can be achieved by reducing wall-normal convection on the suction side using suction. The reduction in  $\delta$  in Fig 4b) indicates a decrease in wall-normal convection. This is consistent with the findings of Atzori *et al.* (2020) showed that a decrease in wall-normal convection directly reduces total drag by substantially reducing pressure drag. This indicates that the baseline  $C_d = 0.009$  of an airfoil at AoA of  $5^\circ$  for  $Re_c = 10^7$  can be reduced by the wavy wall. Although, the exact increase in the lift coefficient  $C_l$  remains undetermined, a tangential shift in the flow separation point quantified as  $\Delta x_{t,s}c^{-1} = 8.3\%$ , where  $c$  is the chord of the applied wing section, can be

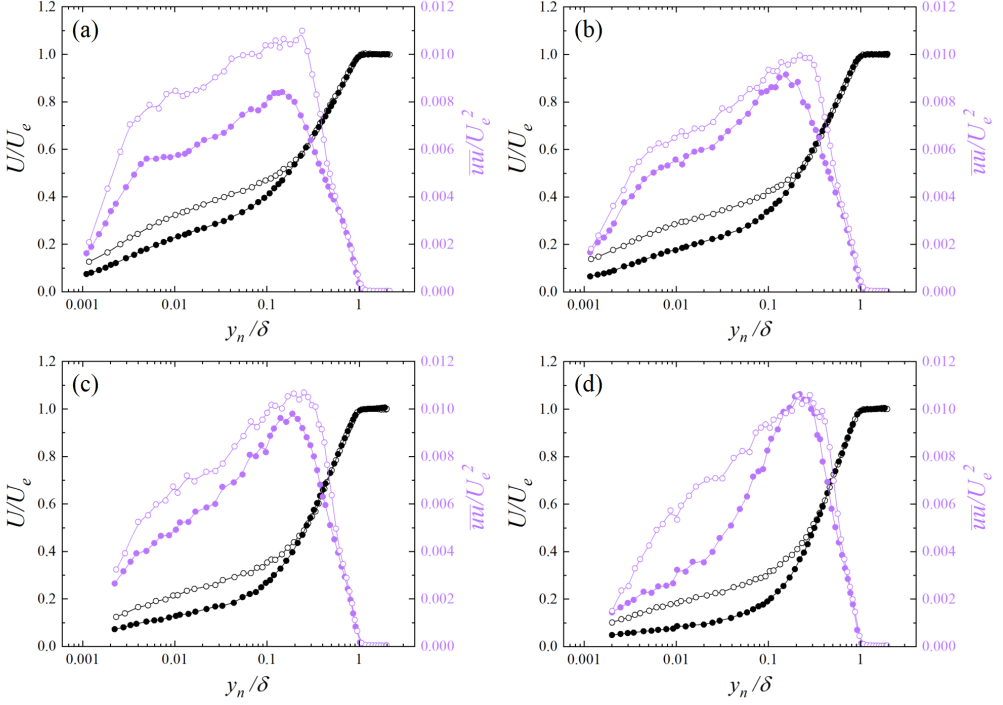


Figure 6: Comparison of the mean velocity and velocity variance components:  $x = 900$  mm a),  $x = 1000$  mm b),  $x = 1100$  mm c) and  $x = 1200$  mm d).

associated with at least 5% increase in lift, which is considered a huge improvement in the aerodynamic performance of the airfoil at this Reynolds number.

The values of  $Re_\theta$  and other important TBL parameters of eleven velocity profiles determined in the flow over the wing section are shown in Table 3. It can be concluded that the optimal configuration causes the local  $Re_\theta$  to decrease when using a wavy wall. Other parameters indicating the effectiveness of the proposed flow control method are presented in Figure 5. The primary parameter most affected is  $\beta$  as it includes the wall shear stress that is strongly influenced (see Figure 5a). The distributions show a considerable decrease in the value of  $\beta$  as a result of the impact of wavy wall. The increase in strain rate, which is proportional to the wall shear stress, is also reflected in the reduction in the thickness of the TBL (see Figure 5b) and in the shape factor  $H$  (see Figure 5c). Interestingly, the Reynolds number  $Re_\tau$  distributions observed above  $\beta \approx 15$  (see Figure 5d) show that the wavy wall do not cause a visible decrease in  $Re_\tau$  downstream of WW.

To confirm the above statement and to gain a more detailed insight into the flow field modified by the wavy wall, the profiles of mean velocity and streamwise Reynolds stress downstream the flow are shown in Figure 6. Note that the profiles are normalised by the edge velocity  $U_e$ . The streamwise evolution of these profiles is shown at the locations  $x = 900$  mm,  $x = 1000$  mm,  $x = 1100$  mm, and  $x = 1200$  mm on the surface. The black symbols correspond to the profiles measured on the unmodified wing surface, while the open symbols represent the profiles for the WW case.

All mean velocity profiles (obtained on the unmodified wing surface and the surface with the wall undulations) collapse in the outer region, which means that the wavy wall only affects the inner region of the boundary layer, where a marked increase in mean velocity is observed.

Table 3: Experimental TBL parameters for unmodified wing and wavy surface

$x\delta_m^{-1}$	$x$	$U_e$	$\delta$	$Re_\theta$	$Re_\tau$	$C_f$	$\delta^*$	$\theta$	$H$	$l^+$
NACA4412 unmodified surface										
3.31	0.30	14.30	98.69	10999	3145	0.00235	16.14	11.83	1.364	38.24
5.52	0.50	13.81	110.67	12816	3098	0.00194	20.35	14.26	1.427	33.59
7.73	0.70	13.25	129.28	15592	3081	0.00153	27.91	18.07	1.544	28.60
9.94	0.90	12.71	154.46	19336	2964	0.00109	41.32	23.55	1.755	23.03
11.05	1.00	12.42	173.07	21310	2930	0.00089	50.71	26.56	1.909	20.31
12.15	1.10	12.27	191.92	23140	2506	0.00055	61.72	29.33	2.105	15.67
13.26	1.20	12.21	213.48	25269	2032	0.00029	76.72	32.19	2.384	11.42
with wavy surface										
9.94	0.90	12.61	148.00	17699	3032	0.00135	37.10	22.47	1.651	8.40
11.05	1.00	12.33	163.90	20349	3108	0.00118	45.95	26.11	1.760	7.78
12.15	1.10	12.49	183.85	23035	3165	0.00097	56.92	29.46	1.932	7.06
13.26	1.20	12.21	201.72	25112	3115	0.00081	66.87	32.63	2.049	6.33

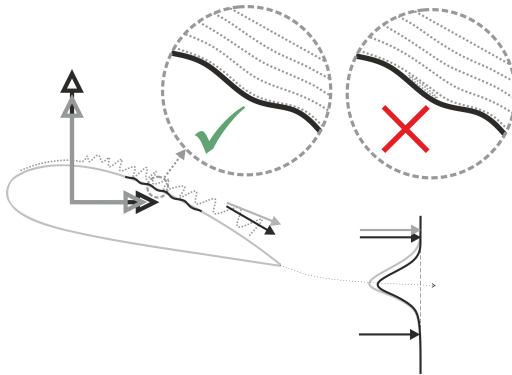


Figure 7: Schematic mechanism of the wavy wall at high Reynolds numbers. The dark colour corresponds to the characteristics (lift force, drag force, and wake) of a wavy wall with a flow at the verge of separation in troughs.

It can be concluded that the characteristic behaviour of the mean profile when we deal with the effective flow control strategy is a decrease in the wake region. Figure 6a at  $x = 900\text{mm}$  shows that the  $\overline{uu}U_e^{-2}$  is leverage due to the wavy wall, and it decays downstream, which is visible for  $x = 1000\text{mm}$  and  $1100\text{mm}$  profiles. For the last profile (Fig. 6d), the level of  $\overline{uu}U_e^{-2}$  for the unmodified case drops significantly, which is caused by the fact that the flow is close to separation. A direct comparison between  $\overline{uu}U_e^{-2}$  profiles indicates that the wavy surface is responsible for flattening the outer maximum. The flattening rate increases with increasing  $x$ . There is also a noticeable increase in  $\overline{uu}U_e^{-2}$  distributions in the near-wall region. This effect can be attributed to the change in the flow history of the pressure gradient, as the distribution  $\beta$  (see Figure 5) is weaker for a wavy wall, causing the outer maximum to shift away from the wall (Bobke *et al.* 2017).

#### 4.2. New insights into physical effects due to wavy wall

Figure 7 presents the mechanism induced by the wavy-wall, provided that there is no flow separation in the trough at a high Reynolds number. This condition promotes the largest difference between the mean flow and the convection of small scales, increasing the sweeping motion, thus the increase in near-wall momentum downstream. This mechanism also reduces wall-normal convection, as indicated by a less deflected velocity vector from the airfoil surface, as evidenced by lower  $\delta$ . It was confirmed by Atzori *et al.* (2020), that the reduced wall-normal convection promotes a momentum redistribution to the near-wall region of the airfoil suction surface, directly decreasing the deficit in the wake of the airfoil. The physical mechanism of an increase in momentum by a wavy wall was discussed in Drózdź *et al.* (2025) in the aspect of small-scale activity. The key condition to promote momentum increasing wavy wall is high energy of small scales over the wavy surface flow without the separation in through. In particular, it was also concluded that the dominant influence of large-scale motions, manifested as an outer peak in the streamwise Reynolds stress that exceeds the energy of the inner peak, indicates a shift of energy across the turbulence scales. When small-scale activity remains elevated, it signifies enhanced momentum transport induced by the wavy wall. The decreasing fraction of small scales below a certain level within the APG flow region defines the efficiency of the wavy wall, which limits the usability of the wavy wall for high values of  $\beta$ . The limiting value of  $\beta$  depends on the effect of the flow history, as the appearance of the outer peak in  $\overline{uu}$  decays with the strength of APG. Under the condition that the evolution of  $\beta$  is slow, the outer peak appears earlier, so the termination of WW should also be earlier, i.e., for the lower  $\beta$  than for strong APGs (Drózdź *et al.* 2025). The WW induced mechanism operates such that, when the limit is defined correctly for a particular flow history and the density of small-scale eddies (Herpin *et al.* 2013) above the wavy wall is sufficiently high, the largest difference between the mean flow and the convection of small scales, increasing the sweeping motion, thus the increase in near-wall momentum downstream. Then the increased momentum from the wavy wall maximises the production of small scales downstream and enhances turbulent mixing, preventing the flow separation. However, this enhancement occurs only when there is no flow separation within the valley (see Fig. 7). So, these conditions defines the proper amplitude and effective slope (ES) of the wavy wall for each wave period. In APG flows with an extensive outer-peak in the streamwise Reynolds stress, large-scale motions dominate the flow, and the wavy-wall mechanism is limited because the small-scale eddy density is insufficient, leading to reduced turbulent mixing and massive separation in the valley. It happens even with the same amplitude and period, but with a high eddy density.

To illustrate this efficiency-limiting mechanism, we consider a configuration in which the wavy wall is extended by one additional period of 0.135 m. Results presented in Figure 8 were obtained for two cases, i.e. for a wavy wall ending at  $\beta \approx 8$  (see Figure 5a) and for the case with the increase of WW by one period, which gives the end of WW at  $\beta \approx 12$ . Additional profiles taken at the unmodified surface were present for comparison at the same location. The comparison of mean velocity profiles and viscous scaled Reynolds stress is presented in Figure 8a) and Figure 8b), respectively. Figure 8a) reveals (see blow-up in the figure) that the velocity deficit for longer WW is greater up to  $y_n \delta^{-1} \approx 50\%$  of the thickness of the TBL, while Figure 8b) shows that the viscous scaled  $\overline{uu}^+$  decreases at the outer peak for both cases of WW, similar to the work of Atzori *et al.* (2020) when suction was implemented on the suction side. Interestingly, for the shorter WW,  $\overline{uu}^+$  is also reduced near the wall, indicating that the method better transports momentum to the wall while simultaneously reducing the universal turbulence level.

A higher velocity deficit indicates a lower increase in the skin-friction coefficient despite

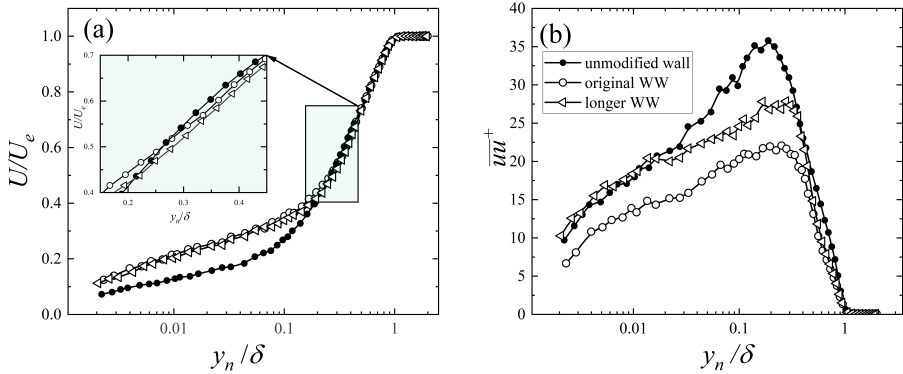


Figure 8: Comparison of the  $U/U_e$  (a) and  $\overline{uu}^+$  (b) components at  $x = 1100$  mm. Symbols as in Figure 6, while results with longer wavy wall are marked with left triangles.

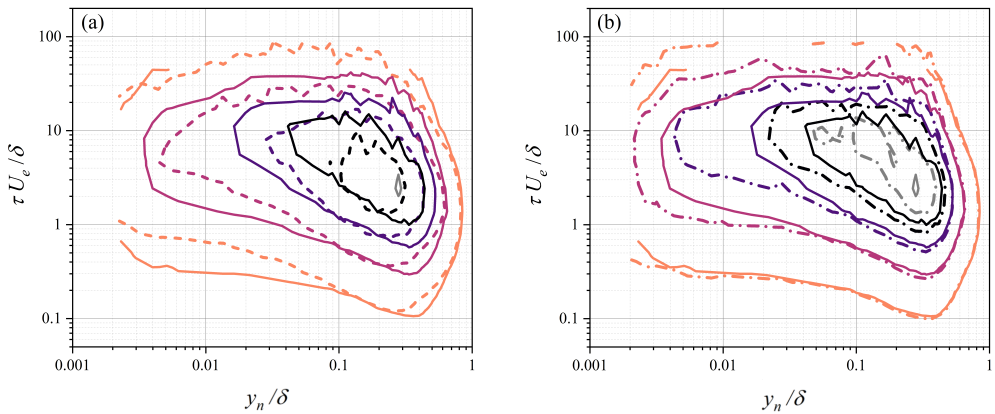


Figure 9: Premultiplied energy spectra comparison at location  $x = 1100$  mm. Solid lines original WW and dashed contours wing profile surface (a) and dashed-dotted contours WW extended by one period (b). Increments marked by colours between iso-contour levels equal 0.0005.

a clear increase in energy throughout the entire boundary layer thickness. To explain the role of small and large scales fractional energy contribution in the flow, the iso-contours of the wavelet energy spectra  $E_{uu}$  (equivalent to the pre-multiplied energy spectra) are presented in Figure 9 for the same location for these cases. The reduced wavelet energy spectra  $E_{uu}U_e^{-2}$  are presented as a function of the normalised time scale  $\tau U_e \delta^{-1}$  and the normalised wall distance  $y\delta^{-1}$ . In Figure 9a), an increase in large-scale energy across the TBL thickness and a small-scale energy increase near the wall due to original WW (solid line) is observed. A similar enhancement of small-scale energy is observed in a longer wavy wall (see dashed-dot line in Figure 9b); however, the higher increase in large-scale energy occurs for that case. It indicates that too high Reynolds stress level (see Figure 8) further downstream of the wavy wall is a result of the large-scale energy instability produced by a too long WW. It indicates that, the reduction in large-scale energy ensures that the argument of Atzori *et al.* (2020) is correct, namely that a net reduction in drag — manifested by delayed separation, decreased wake strength, and lower drag coefficient — is achievable only due to the decrease of large-scale energy accompanied by the skin-friction coefficient increase on the suction side of the

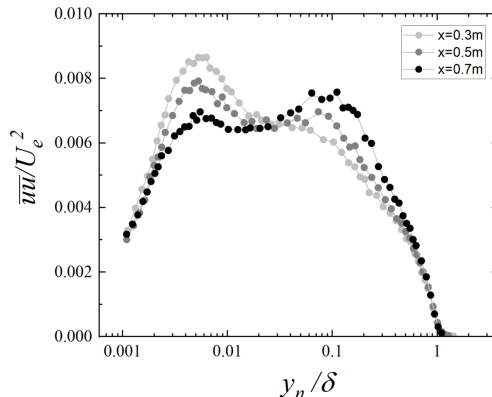


Figure 10: Normalised variance distribution over the measurement domain (300 mm to 700 mm)

airfoil. Conversely, an amplification of large-scale energy leads to intensified mixing in the wake region, thereby undermining the efficacy of the flow control strategy.

The effect discussed above explains specific differences between the experimental and numerical results in assessing how the wavy wall affects the flow structures. The numerical simulations of Kamiński *et al.* (2025) report a distinct increase in large-scale energy observed in the velocity premultiplied spectra distributions attributed to the WW effect. However, in the numerical study (Kamiński *et al.* 2024; Kamiński *et al.* 2025), the WW extended to  $\beta \approx 10$ , which was accepted according to the first studies of Drózdź *et al.* (2021). In the current experimental setup, the WW terminates earlier at  $\beta \approx 8$ , which is consistent with the earlier outer-peak enhancement (see profile  $x = 0.7$  m in Fig. 10 in Appendix 1). Furthermore, the final period of WW in the numerical case exhibited an amplitude exceeding  $A^+ = 170$ , according to the early experimental results, resulting in a decrease in control efficiency and substantial large-scale production. In summary, excessively long WW and too high amplitudes may trigger large-scale instability, providing minimal benefits and reducing the efficiency of the WW mechanism. These findings emphasise that an optimally designed WW enhances the population of small-scale structures without contributing to large-scale energy production. Although the first studies of Drózdź *et al.* (2021) suggested terminating WW at  $\beta \approx 10$ , however, as shown in subsequent studies Drózdź *et al.* (2025), this threshold is not strictly governed by the value of  $\beta$ . Instead, the decisive criterion is the emergence of a distinct outer peak in Reynolds stress that exceeds the inner peak:  $\max(\overline{u u}_{\text{outer}}) > \max(\overline{u u}_{\text{inner}})$ . According to that criterion, location  $x = 700\text{mm}$  is the limit for WW application for the case analysed in the paper (see Figure 10). Upstream of this location, the inner peak (indicating small-scale activity) dominates near the wall. Exceeding the above limit (uu.uu) marks a shift in the dominant mechanism of turbulence production. Beyond this point, the effectiveness of WW in controlling flow separation diminishes, and the momentum-loss thickness increases. The recommendation for other cases where the flow history differs, leading to other locations where the outer peak in the streamwise Reynolds stress profile overtakes the inner peak.

Therefore, an optimal WW design should maintain small-scale universality by minimising excessive Reynolds stress in the outer layer. By tracking the evolution of turbulent structures, particularly when the outer peak surpasses the inner peak, the streamwise extent of the WW can be fine-tuned to maximise control efficiency without inducing large-scale instabilities. Conversely, if this limit is exceeded, large-scale motions become dominant, suppressing

the enhancement of small-scale propagation speed and resulting in higher momentum-loss thickness.

## 5. Conclusions and discussions

A detailed experimental study shows that the addition of a wavy wall to a convex surface, in the specified location, may constitute a previously unexamined passive method to alter aerodynamic behaviour. It provides a new approach to delay flow separation and improve airfoil performance at high Reynolds numbers.

The presence of the wavy surface leads to a substantial rise in the skin-friction coefficient. Comparative results show that the selected corrugation shape may produce even a 42.3% increase over the integration region extending from the end of the wavy wall to the location where separation would begin on a smooth, unmodified surface. A significant outcome is the tangential shift in the flow separation point by 8.3% of the chord, which is roughly associated with about a 5% increase in lift for an airfoil at the given Reynolds number. This represents a substantial improvement in aerodynamic performance, primarily due to sustained momentum loss thickness and a 5% reduction in turbulent boundary layer thickness, indicating that the wall-normal convection is decreased due to an increase of streamwise convection caused by the wavy wall. Mean velocity profiles show a notable increase in the inner part, along with a noticeable rise in Reynolds stress distributions and flattening of the outer maximum due to waviness occupying the near-wall region. Furthermore, an increase in strain rate also contributes to a reduction in the shape factor  $H$ . At the same time, the value of  $Re_\tau$  remains at a constant level further downstream of the wavy wall, contrasting with observations on the unmodified section of the wing.

The comprehensive analysis of the presented research also sheds light on the mechanisms by which wavy surfaces influence aerodynamics, which are now better understood and emphasise the significant role of small-scale turbulence. The fundamental feature driving the momentum towards the wall increase is small-scale turbulent activity. The wavy wall works effectively when a high concentration of small-scale eddies is present above its surface, enhancing small-scale convection along the downhill side, as long as flow separation does not occur within the valleys. However, the wavy wall's efficacy is critically bound. Its benefits diminish at high  $\beta$  values, where large-scale motions become dominant. The presented results indicate, that the excessive length of the wavy wall can trigger detrimental large-scale instability, reducing WW efficiency in enhancing momentum-increasing sweep events. The optimal termination criterion for a wavy wall is not a fixed  $\beta$  value, as previously thought, but rather flow history, which is evidenced by the emergence of a distinct outer peak in the Reynolds stress that surpasses the inner peak. Beyond this point, the wavy wall's ability to control flow separation diminishes, and the momentum-loss thickness increases. Excessive wavy wall amplitude will have a similar effect. This reinforces the conclusion that maintaining the small-scale eddy density high is the primary determinant of wavy wall effectiveness and superior momentum transport.

In essence, the wavy surface, when precisely tuned, acts as a sophisticated flow control mechanism, effectively increasing skin friction and postponing flow separation, thus enhancing lift without a detrimental impact on overall airfoil drag, through favourable modifications to the boundary layer structure and momentum management.

Future studies will investigate the enhanced performance achieved by introducing a non-harmonic wave type to a curved surface resembling a blade surface.

**Funding.** The investigation was supported by National Science Centre under Grant No. DEC-2020/39/B/ST8/01449.

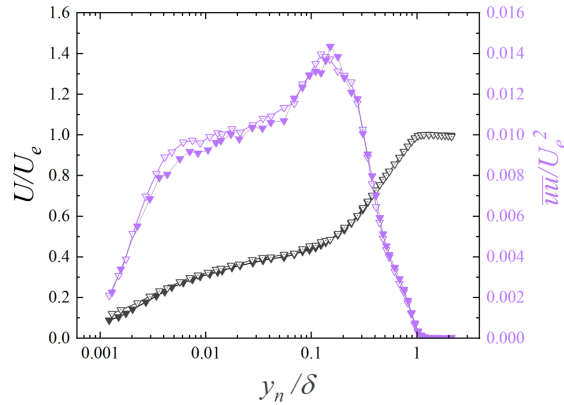


Figure 11: Comparison between two types of hot-wire probes of the mean velocity and velocity variance components at  $x = 900$  mm of the longer wavy wall. The open triangle corresponds to the gold-plated hot-wire probe 55P05. The dark triangle corresponds to modified hot wire 55P31 measurements.

**Declaration of interests.** The authors report no conflict of interest.

**Data availability statement.** The data that support the findings of this study are openly available in [RepOD] at <https://doi:10.18150/6BIJJK>, reference number [doi:10.18150/6BIJJK](https://doi:10.18150/6BIJJK)

**Author ORCIDs.** A. Drózdź, <https://orcid.org/0000-0002-8521-028X>; M. Romańczyk, <https://orcid.org/0000-0002-5198-5490>; W. Elsner, <https://orcid.org/0000-0003-2881-2783>

**Author contributions.** Artur Drózdź: Writing – original draft, Writing – review and editing, Visualisation, Validation, Supervision, Software, Methodology, Investigation, Formal analysis, Data curation, Conceptualisation. Mathias Romańczyk: Methodology, Investigation, Visualisation, Validation. Witold Elsner: Writing – review and editing, Supervision, Resources, Project administration, Investigation, Funding acquisition, Formal analysis, Conceptualisation, Validation.

## Appendix A.

In the appendix, the effects of hot-wire spatial averaging are discussed. According to Drózdź *et al.* (2024), the hot-wire spatial averaging in APG flows in the inner and outer peaks in streamwise Reynolds stress  $\overline{uu}$  can be observed up to  $\beta = 20$  due to a too long sensing length of the hot-wire. Above that value of  $\beta$ , the length of the wire of 100 viscous units gives an attenuation lower than the uncertainty of 5%. The critical location for analysed data is location  $x = 900$  mm for  $\beta \approx 15$ , where  $l^+ = 23$  (see Table 3). To show the estimation reliability of the  $\overline{uu}$  Reynolds stresses for the two probes, gold-plated and modified, were compared in Figure 11 for the case with a longer wavy wall that produces slightly higher wall shear stress than the unmodified surface. The results reveal a discrepancy between profiles within the uncertainty range.

In the analysis, the crucial location is  $x = 700$  mm at  $\beta \approx 8$  and  $l^+ = 29$ , where the outer peak dominates. The verification must be performed to check if the attenuation at the inner peak of  $\overline{uu}$  is not higher than at the outer peak. Again, according to Drózdź *et al.* (2024), the attenuation in  $\Delta\overline{uu}^+$  at the outer peak is twice as high at the inner peak, but still, as the  $l^+$  is relatively short, the attenuation is within the uncertainty range, which in the aspect of the wavy wall termination, it proves that the location is correct.

The attenuation is relatively high for the two remaining locations  $x = 300$  and  $500$  mm, as  $l^+$  is 38 and 34, respectively. Assuming linear attenuation with  $l^+$ , it can be said that both are

at the attenuation level of 40% of those presented in Drózdź *et al.* (2024). Then, the outer peak of  $\overline{uu}$  is attenuated at about 4% (still in uncertainty range) and as high as 16% in the inner peak of  $\overline{uu}$ .

## REFERENCES

- AOKI, K., MUTO, K. & OKANAGA, H. 2012 Mechanism of drag reduction by dimple structures on a sphere. *Journal of Fluid Science and Technology* **7** (1), 1–10.
- ATZORI, MARCO, VINUESA, RICARDO, FAHLAND, GEORG, STROH, ALEXANDER, GATTI, DAVIDE, FROHNAPFEL, BETTINA & SCHLATTER, PHILIPP 2020 Aerodynamic Effects of Uniform Blowing and Suction on a NACA4412 Airfoil. *Flow, Turbulence and Combustion* **105**, 735–759.
- BEARMAN, P. W & HARVEY, J. K 1976 Golf ball aerodynamics. *Aeronautical Quarterly* **27** (2), 112–122.
- BELAMADI, R., DJEMILI, A.B, ILINCA, A. & MDOUKI, R. 2016 Aerodynamic performance analysis of slotted airfoils for application to wind turbine blades. *Journal of wind engineering and industrial aerodynamics* **151**, 79–99.
- BOBKE, A., VINUESA, R., ÖRLÜ, R. & SCHLATTER, P. 2017 History effects and near equilibrium in adverse-pressure-gradient turbulent boundary layers. *Journal of Fluid Mechanics* **820**, 667–692.
- BRAVO-MOSQUERA, P. D., CATALANO, F. M. & ZINGG, D. W. 2022 Unconventional aircraft for civil aviation: A review of concepts and design methodologies. *Progress in Aerospace Sciences* **131** (December 2021).
- CODER, J. G & SOMERS, D. M 2020 Design of a slotted, natural-laminar-flow airfoil for commercial transport applications. *Aerospace Science and Technology* **106**, 106217.
- DRÓZDŹ, A., NIEGODAJEW, P., ROMAŃCZYK, M. & ELSNER, W. 2023 Convection velocity in turbulent boundary layers under adverse pressure gradient. *Experimental Thermal and Fluid Science* p. 110900.
- DRÓZDŹ, A., NIEGODAJEW, P., ROMAŃCZYK, M., SOKOLENKO, V. & ELSNER, W. 2021 Effective use of the streamwise waviness in the control of turbulent separation. *Experimental Thermal and Fluid Science* **121**, 110291.
- DRÓZDŹ, A., ÖRLÜ, R., SOKOLENKO, V., SCHLATTER, P., ELSNER, W. & NIEGODAJEW, P. 2024 Hot-wire spatial resolution issues in adverse pressure gradient turbulent boundary layers. *Measurement* **237**, 115229.
- DRÓZDŹ, A., SOKOLENKO, V. & ELSNER, W. 2025 Performance analysis of novel wavy-wall-based flow control method for wind turbine blade. *Experimental Thermal and Fluid Science* **169** (March), 111527.
- ELSNER, W., DRÓZDŹ, A., SZYMANEK, E., TYLISZCZAK, A. & NIEGODAJEW, P. 2022 Experimental and numerical studies of turbulent flows over two-dimensional and three-dimensional rough surfaces under an adverse pressure gradient. *Applied Mathematical Modelling* **106**, 549–566.
- GATTERE, F., CHIARINI, A.O & QUADRIO, M. 2022 Dimples for skin-friction drag reduction: status and perspectives. *Fluids* **7** (7), 240.
- HERPIN, S., STANISLAS, M., FOUCAUT, J. M. & COUDERT, S. 2013 Influence of the reynolds number on the vortical structures in the logarithmic region of turbulent boundary layers. *Journal of Fluid Mechanics* **716**, 5–50.
- KAMIŃSKI, P., TYLISZCZAK, A. & ELSNER, W. 2025 Turbulent separation control on an airfoil surface using a wavy wall. *Phys. Fluids* **37** (April), 075157.
- KAMIŃSKI, P., NIEGODAJEW, P., DRÓZDŹ, A., SOKOLENKO, V., TYLISZCZAK, A. & ELSNER, W. 2024 Numerical analysis of novel wavy wall based control of turbulent boundary layer separation. *Aerospace Science and Technology* **149**, 109167.
- KAMIŃSKI, P., TYLISZCZAK, A., ELSNER, W. & NIEGODAJEW, P. 2025 Turbulent separation control with a tilted wavy wall: A promising approach for energy savings in aerodynamic systems. *Energy* **324**, 135758.
- MATHIS, R., MONTY, J. P, HUTCHINS, N. & MARUSIC, I. 2009 Comparison of large-scale amplitude modulation in turbulent boundary layers, pipes, and channel flows. *Physics of Fluids* **21** (11), 111703.
- MCMASTERS, J. H & HENDERSON, M. L 1979 Low-speed single-element airfoil synthesis. *NASA. Langley Res. Center The Sci. and Technol. of Low Speed and Motorless Flight, Pt. 1*.
- MONKEWITZ, P. A., CHAUHAN, KAPIL A. & NAGIB, HASSAN M. 2007 Self-consistent high-reynolds-number asymptotics for zero-pressure-gradient turbulent boundary layers. *Physics of Fluids* **19** (11), 115101, arXiv: [https://pubs.aip.org/aip/pof/article-pdf/doi/10.1063/1.2780196/16088212/115101\\_1\\_online.pdf](https://pubs.aip.org/aip/pof/article-pdf/doi/10.1063/1.2780196/16088212/115101_1_online.pdf).
- MOSTAFA, W., ABDEL SAMIE, A., SEDRAK, M., THÉVENIN, D. & M., M. H 2022 Quantitative impact of a

- micro-cylinder as a passive flow control on a horizontal axis wind turbine performance. *Energy* **244**, 122654.
- NIEGODAJEW, P., DRÓZDZ, A. & ELSNER, W. 2019 A new approach for estimation of the skin friction in turbulent boundary layer under the adverse pressure gradient conditions. *International Journal of Heat and Fluid Flow* **79**, 108456.
- RICCO, P., SKOTE, M. & LESCHZINER, M. A. 2021 A review of turbulent skin-friction drag reduction by near-wall transverse forcing. *Progress in Aerospace Sciences* **123**, 100713.
- S., SEONG-HO & H., CHEOL-HYUN 2016 Performance improvement of airfoils for wind blade with the groove. *International Journal of Green Energy* **13** (1), 34–39, arXiv: <https://doi.org/10.1080/15435075.2014.910777>.
- SANMIGUEL VILA, C., VINUESA, RICARDO, DISCETTI, S., IANIRO, A., SCHLATTER, P. & ÖRLÜ, RAMIS 2017 On the identification of well-behaved turbulent boundary layers. *J. of Fluid Mech.* **822** (May), 109–138.
- SAYED, M. A., KANDIL, HAMDY A. & MORGAN, EL-SAYED I. 2012 Computational fluid dynamics study of wind turbine blade profiles at low reynolds numbers for various angles of attack. *AIP Conference Proceedings* **1440**, 467 – 479, cited by: 3.
- TANÜRÜN, H. E., YILDIZ, A. & SEYHAN, M. 2026 Aerodynamic performance analysis of a naca 63(4)-421 airfoil equipped with a trailing edge slot at suction side. *Experimental Thermal and Fluid Science* **171**, 111604.
- TAY, C 2011 Determining the effect of dimples on drag in a turbulent channel flow. In *49th AIAA Aerospace Sciences Meeting Including the New Horizons Forum and Aerospace Exposition*, p. 682.
- TAY, CMJ, KHOO, BC & CHEW, YT 2015 Mechanics of drag reduction by shallow dimples in channel flow. *Physics of Fluids* **27** (3).
- WANG, J.-S., WU, J. & WANG, J.-J. 2023 Wake-triggered secondary vortices over a cylinder/airfoil configuration. *Experiments in Fluids* **64** (1), 6.
- WANG, Y., LI, G., S.SHEN, HUANG, D. & ZHENG, Z. 2018 Influence of an off-surface small structure on the flow control effect on horizontal axis wind turbine at different relative inflow angles. *Energy* **160**, 101–121.